PCCP

ROYAL SOCIETY OF CHEMISTRY

ARTICLE TYPE

Cite this: DOI: 10.1039/xxxxxxxxxx

Photodissociation dynamics of CH_3I probed via multi-photon ionisation photoelectron spectroscopy.

Emily M. Warne,[†a] Briony Downes-Ward,[†a] Joanne Woodhouse,[a] Michael A. Parkes,[b] Darren Bellshaw,[c] Emma Springate,[d] Paulina Majchrzak,[d] Yu Zhang,[d] Gabriel Karras,[d] Adam Wyatt,[d] Richard T. Chapman,[d] Adam Kirrander,[c] and Russell S. Minns*[a]

Received Date
Accepted Date

DOI: 10.1039/xxxxxxxxxx

www.rsc.org/journalname

The dissociation dynamics of CH_3I are investigated on the red (269 nm) and blue (255 nm) side of the absorption maximum of the A-band. Using a multiphoton ionisation probe in a time-resolved photoelectron imaging experiment we observe very different dynamics at the two wavelengths, with significant differences in the measured lifetime and dynamic structure. The differences are explained in terms of changes in excitation cross-sections of the accessible $^3Q_0$ and $^1Q_1$ states and the subsequent dynamics upon each of them. The measurements support the existing literature on the rapid dissociation dynamics on the red side of the absorption maximum at 269 nm which is dominated by the dynamics along the $^3Q_0$ state. At 255 nm we observe similar dynamics along the $^3Q_0$ state but also a significant contribution from the $^1Q_1$ state. The dynamics along the $^1Q_1$ potential show a more complex structure in the photoelectron spectrum and a significantly increased lifetime, indicative of a more complex reaction pathway.

Introduction

UV excitation into the A-band of CH_3I typically leads to rapid photodissociation, which has been the subject of numerous studies in both the time and frequency domains; see for example ref[1–10] and ref[11–17] respectively, and references therein. The A-band absorption is dominated by the σ^*(C-I) $\leftarrow$ n(I) transition, leading to a weakening of the C-I bond following promotion of a non-bonding electron from the iodine atom into an antibonding orbital associated with the C-I bond.[13] The subsequent dynamics can be understood with reference to Fig. 1. Close to the absorption maximum, the $\sigma^* \leftarrow$ n transition predominantly populates the $^3Q_0$ excited state via a strong parallel transition. The $^3Q_0$ excited state is asymptotically linked to fragments associated with the upper spin orbit state of iodine, $I(^2P_{1/2})$, in conjunction with the $CH_3(X)$ radical in its electronic ground state.[18] A conical intersection between the $^3Q_0$ and $^1Q_1$ states allows for efficient population transfer between the two as the molecule dissociates. The $^1Q_1$ state is one of two other, weaker, perpendicular transitions whose absorption maxima are in the wings of the overall A-band absorption spectrum, with a $^3Q_1$ state maximum lying to the red side of the absorption maximum and the $^1Q_1$ lying to the blue side. Both states correlate with the ground spin-orbit state of iodine, $I(^2P_{3/2})$, and the ground electronic state of the CH_3 radical as dissociation products. The relative contributions of these states to the total absorption spectrum is somewhat uncertain. Experimental measurements of product state angular distributions by Eppink and Parker[12] suggest the contributions are very small relative to the dominant $^3Q_0$ state across the majority of the absorption band. Contrary to this, magnetic circular dichroism (MCD) measurements indicate the contributions from the blue-shifted $^1Q_1$ state can be significant,[11] on the order of 20% of the absorption maximum, with a number of predictions of the absorption spectrum based on potential energy surfaces showing similar cross-sections to the MCD measurement.[14,19] The contribution of the red-shifted $^3Q_1$ state is also unclear, with theory[14,19] predicting a much higher relative cross-section than seen in the MCD experiments[11] or the product distributions measured by Eppink and Parker.[12]

In the following, we report a time-resolved photoelectron imaging study of the dissociation dynamics of methyl iodide. We compare the dynamics upon slightly red and blue shifted excitation relative to the absorption maximum, at 269 nm and 255 nm respectively, observing significant differences in the measured spectrum and dynamics that are indicative of different excitation fractions and dissociation pathways.

Existing Energy-resolved measurements of A-band dissociation

[a] Chemistry, University of Southampton, Highfield, Southampton SO17 1BJ, UK.
[b] Department of Chemistry, University College London, 20 Gordon Street, London.
[c] EaStCHEM, School of Chemistry, University of Edinburgh, David Brewster Road, EH9 3FJ Edinburgh
[d] Central Laser Facility, STFC Rutherford Appleton Laboratory, Didcot, Oxfordshire OX11 0QX, UK.
† These authors contributed equally to this work.
* email: r.s.minns@soton.ac.uk

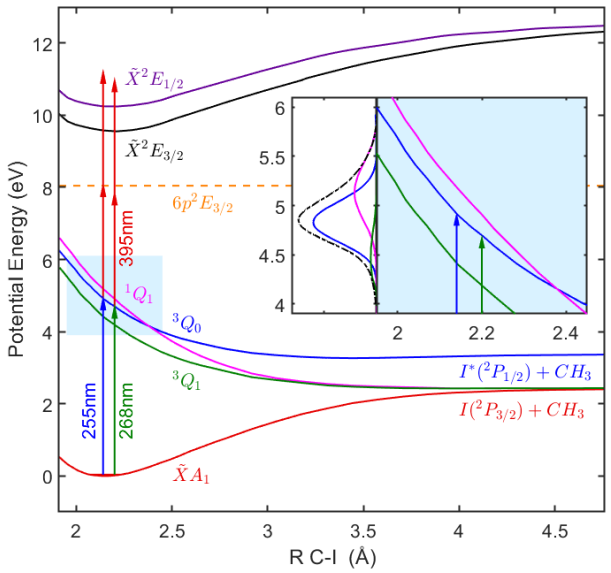

Fig. 1 1-D cuts along the C-I dissociation coordinate of the potential energy surfaces of CH_3I relevant to the UV photodissociation and photoelectron detection scheme used, adapted from ref[20,21]. Inset: expanded figure of the excited state potentials and a breakdown of the absorption spectrum into contributions from the three Q states associated with the A-band absorption as a function of energy based on ref[19]

have focused on the product state and angular distributions of the final methyl and iodine products.[12–15] The high levels of alignment in the dissociation products provide evidence for the rapid and efficient dissociation of CH_3I at many wavelengths. Angular distributions of the methyl and iodine fragments measured by Eppink and Parker[12] at a number of discrete wavelengths across the A-band have been used to quantify the level of excitation into the three accessible states by taking into account the parallel and perpendicular character of the excitation. The highly parallel distributions of the products formed were used to extract excitation cross-sections for the $^1Q_1$ and $^3Q_1$ states, giving values of less than 1% of the absorption maximum of the $^3Q_0$ state. The angular distributions showed that the majority of the products, including both the ground and excited states of iodine, are predominantly formed following initial excitation to the $^3Q_0$ state. Significant contributions from the $^3Q_1$ state were not observed until well into the wings of the absorption band at wavelengths greater than 295 nm. The analysis contained two main assumptions: that any initial excitation of the perpendicular states does not undergo curve crossing and contribute to the excited state product formation; and that the perpendicular transition would give rise to limiting β_2 values of -1. Should either of these assumptions be unreliable the contribution of the perpendicular states would be underestimated. Bañares and co-workers[15] have subsequently shown the importance of the $^1Q_1$ state on the blue edge of the absorption band. Products formed following initial population of the $^1Q_1$ state dominate the ground state dissociation products for wavelengths below 225 nm and contribute significantly to the excited state products at wavelengths below 220 nm indicating significant population transfer from the $^1Q_1$ state to the $^3Q_0$ state.

Complementary time-resolved measurements[1–10] have concentrated on excitation wavelengths on the red side of the absorption maximum, typically around 266 nm corresponding to the third harmonic of a typical Ti:Sapphire femtosecond laser system. Each measurement provides a consistent picture of the dynamics, with excitation dominated by the $^3Q_0$ state leading to rapid dissociation. Excited state iodine fragments dominate the dissociation yield accounting for approximately 70%[12,19] of all fragments with a measured formation time of around 84 fs.[2] A fraction of the excited state population undergoes internal conversion at a conical intersection leading to the formation of ground state iodine fragments with a yield around 30% and a slightly longer formation time of 94 fs.[2] The transition-state region between the bound molecule and radical fragments has also been studied via femtosecond XUV transient absorption,[3] and core shell spectroscopy,[9] with the structural dynamics probed using laser driven Coulomb explosion imaging.[4,8,10] All of these measurements, however, have been performed to the red of the absorption maximum at wavelengths where the dominant transition is to the $^3Q_0$ state. The generality of the dynamics across the full absorption band and the link to frequency resolved measurements at other wavelengths is therefore unclear. Moreover, the energy region between 240-260 nm is comparatively unexplored experimentally in both the time *and* frequency domains.

Experimental Details

We perform time-resolved photoelectron imaging experiments on the excited state dynamics of CH_3I at two pump wavelengths as outlined in Fig. 1. The wavelengths are chosen such that one wavelength (269 nm, 4.61 eV) is to the red side of the absorption maximum, where experiment suggests the excitation is dominated by population of the $^3Q_0$ state, and the second is to the blue side of the absorption maximum (255 nm, 4.86 eV), where some population of the $^1Q_1$ state may be expected as well as the $^3Q_0$ state. The relative excitation fractions as a function of wavelength are shown in the inset of Fig. 1 based on the calculations of ref[19], however as we have described above, there is significant uncertainty about the relative excitation fractions in the literature.

The majority of the laser and vacuum systems have been described previously[22–24] with only small differences to the overall set-up briefly described here. The pump wavelengths, 255 nm and 269 nm, are generated by a high energy OPA (HE-TOPAS) pumped by 8 W of 790 nm light from the amplified output of a femtosecond laser system (KM labs, Red Dragon). We ionise the excited state population through two-photon absorption of 395 nm light produced by second-harmonic generation of the 790 nm fundamental output of the amplifier. The ionisation energy is sufficient to allow ionisation into both spin-orbit states of the electronic ground state of the CH_3I^+ cation. The laser pulse energy at each of the pump wavelengths is 6 μJ (269 nm) and 1 μJ (255 nm), while the probe is held at 10 μJ. The pump and probe beams are reflection focused into the interaction region with 1 m long focal length optics. We rule out multiphoton

excitation as a potential origin of our dynamic signals through analysis of the spectral and temporal behaviour. Multiphoton excitation with the probe before time zero would populate the B-state which has a ps lifetime. No signals with such long lifetimes are observed. Two photon absorption of the pump at 255 nm would excite above the ionisation potential, populating a vibrational state near the minimum of the ion state potential well. The low energy peaks associated with this are seen as a stationary background which is removed via the background subtraction. No signatures of further absorption of the pump are observed. Preliminary measurements using a femtosecond extreme ultraviolet pulse for single photon ionisation of the excited state show similar time dependent shifts and changes in lifetime. These complementary measurements, which will be the subject of a future publication, provide further reassurances that the dynamic signals are not the result of spurious multiphoton contributions.

The CH_3I molecular beam is created by expanding the room temperature vapour of liquid CH_3I through a kHz pulsed nozzle (Amsterdam Cantilever[25]) with a 200 μm aperture. The molecular beam is skimmed before crossing the laser beams at the centre of the velocity map imaging spectrometer interaction region as described in ref[24]. The photoelectron spectrum and angular distributions are obtained from the raw images through polar onion peeling and scaling with the appropriate Jacobian. The single colour (pump only and probe only) contributions to the spectrum are removed from the data by subtracting the spectrum from the earliest pump-probe delays (probe before pump) from all subsequent photoelectron spectra. The low pressure room temperature expansion minimises any dimer formation and we see no evidence for dimers in the photoelectron spectra obtained.

Results

In Fig. 2(a) we plot the photoelectron spectrum obtained at zero delay between the pump and the probe following excitation with 269 nm light and ionisation with two 395 nm photons. The spectrum is plotted as a function of binding energy as defined by the total photon energy minus the measured electron kinetic energy, to allow for a direct comparison with the spectrum obtained at 255 nm. Combs above the spectrum mark the position of a number of cation states, based on the known ionisation limits and vibrational frequencies of the spin-orbit states of the ground CH_3I^+ cation state.[26,27] The uneven intensity distribution between the two spin-orbit ion states is contrary to single-photon ionisation measurements of the excited states performed with femtosecond XUV sources which show broadly similar intensities for the two spin orbit states following ionisation.[28] The higher intensity into the upper spin-orbit cation state at 10.1 eV when ionising with two photons is therefore surprising and we believe due to a, as yet unidentified, resonant intermediate in the two-photon ionisation step. The 255 nm spectrum in Fig. 2(b) shows the equivalent time-zero ($\Delta t = 0$) spectrum in red. The broad assignment of features is the same except for a broad peak at 10.3 eV which is labelled with a star. We assign this to ionisation into the $\nu_1 = 2$ or $\nu_4 = 2$ of the $^2E_{3/2}$ cation state due to an accidental resonance with the equivalent vibrational states of the 6p Rydberg state at

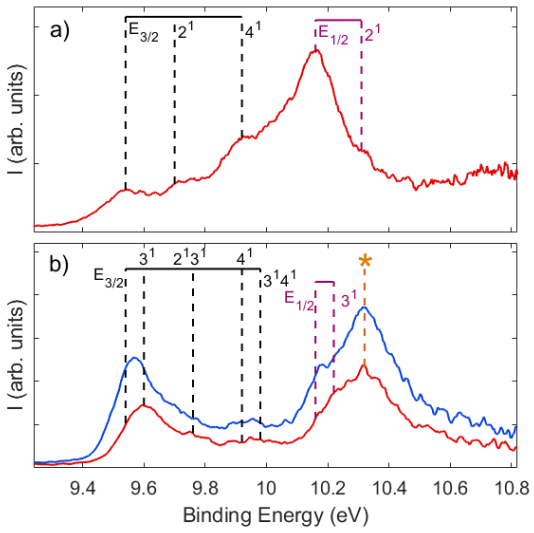

Fig. 2 Photoelectron spectrum obtained at a pump wavelength of 269nm (a) and 255 nm (b) and probed with two 395 nm photons. The photoelectron spectrum obtained at zero time delay is plotted in red in both spectra, while the spectrum obtained at a delay of 100 fs after the 255 nm pump is plotted in blue. Combs mark the position of vibrational states in the lower (black) and the upper (purple) spin orbit states of the ion.

the 1 + 1' level.[29] The energy also matches that expected for ionisation into the $\nu_2 = 1$ vibrational level of the $^2E_{1/2}$ electronic state but it is not clear why this would appear with such an enhanced yield. Resonance-enhanced ionisation through the 6p Rydberg state could explain the enhanced intensity above what may be expected, but this assignment should be considered tentative due to the lack of vibrational resolution in the presented spectrum. However, this assignment is supported by the β-parameters and energy spectrum (see discussion of Figs. 4 and 6).

The full time-dependent photoelectron spectra for both wavelengths are plotted in Fig. 3 where a number of significant differences are apparent. The 269 nm trace plotted in Fig. 3(a) shows a very short-lived signal across all features in the spectrum. Each peak in the spectrum shows the same time dependence and no observable shifts in the energy or peak positions. By comparison, the features in the 255 nm spectrum, Fig. 3(b), show an extended lifetime and shifts in the positions of the maxima in the spectrum to lower binding energies with increasing pump-probe time delay. To highlight the shift, we plot the photoelectron spectrum obtained following 255 nm excitation at time-zero (red) and at a delay of 100 fs (blue) in Fig. 2(b). The time-zero spectrum has an onset that matches the vibrationless level of the cation but peaks around the binding energy associated with $\nu_3 = 1$ vibrational level in both spin-orbit states. At longer times the spectrum is seen to shift to lower binding energy, highlighted in Fig. 3(b) by arrows, to positions more closely matching the expected energy for ionisation into the vibrationless ground state. The shift does not move to match the expected peak position, but the lack of vibrational resolution means the shift is due to an increase in the relative proportion of the ionisation process leading to the vibrationless ground state. This suggests that there is a change in

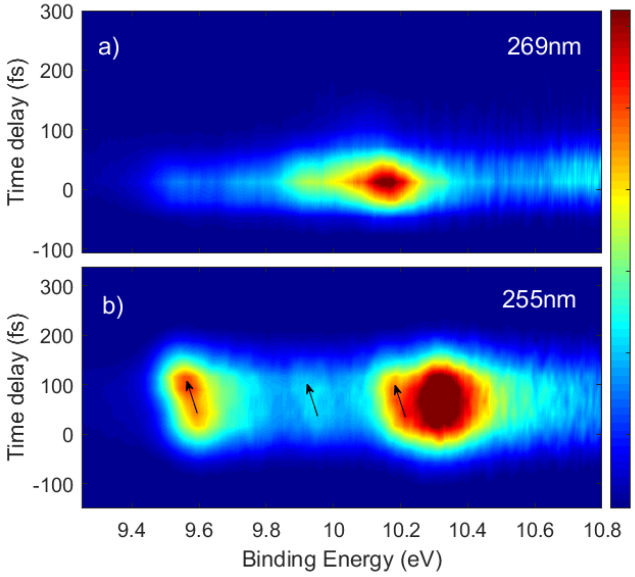

Fig. 3 Time dependent photoelectron spectrum of CH_3I following excitation at 269 nm (a) and 255 nm (b).

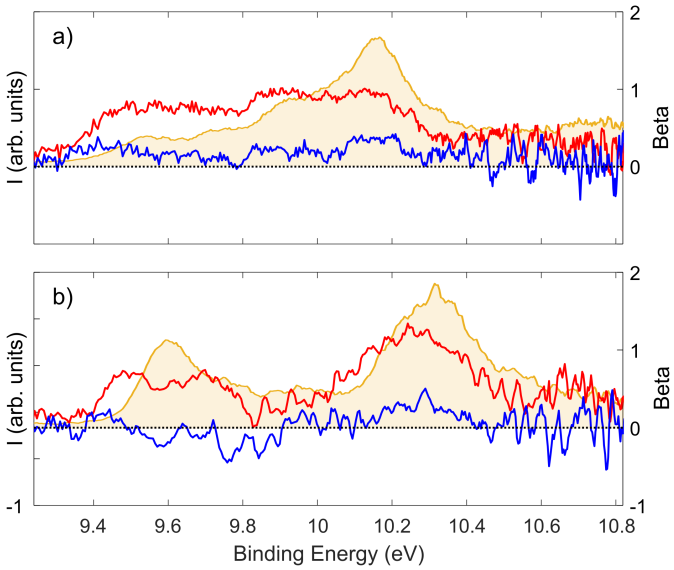

Fig. 4 Photoelectron spectra (yellow) and angular distributions obtained for zero delay between the pump and probe with the 269 nm pump (a) and 255 nm pump (b). In both (a) and (b) β_2 (red) and β_4 (blue) are plotted with the scale on the right hand axis.

vibrational overlap between the excited wavepacket and the vibrational states of the cation over the course of the first 100 fs.

The photoelectron angular distributions were also collected and the obtained beta parameters for the time-zero spectrum are presented in Fig. 4 for the 269 nm (a) and 255 nm (b) pump wavelengths. As excitation and ionisation is a three photon process with each pulse having linear parallel polarisations, we include β_2, β_4 and β_6 in our angular distribution fitting functions used for inversion. The obtained beta parameters do not show any time dependence and therefore provide little information about the dynamics of the system. For both wavelengths the β_6 values are close to zero for all energies and are therefore not presented. At both wavelengths the β_2 values are positive across the full spectrum, with the main peaks showing values close to one, such that the peaks are dominated by contributions in the same direction as the laser polarisation. The β_2 values over the peak assigned to ionisation through a Rydberg intermediate are consistent with those associated with ionisation of the 6p orbital in atomic iodine. The β_4 values are consistent across the 269 nm spectrum with positive values of approximately 0.2-0.3, indicating that the excited-state orbital being ionised is not isotropic and may be considered aligned with respect to the ionising light. There is more variance in the 255 nm spectrum, however it is difficult to know how much significance to place on this considering the low magnitude and variation across the features in the spectrum. Considering the A_1 symmetry in the C_{3v} point group of the possible excited states, one would expect parallel photoelectron angular distributions with near zero β_4 values regardless of any alignment in the excitation step. The photoelectron angular distributions therefore do not reveal the parallel or perpendicular character of the states populated directly. Even in a situation where the any alignment signal remained, the overlapping nature of the bands would make deconvoluting the contributions from each state to the total photoelectron angular distributions challenging. We therefore cannot extract excitation fractions directly from the measurement of the photoelectron angular distribution alone.

To obtain decay associated spectra (DAS), which provide a quantitative description of the changes over the full spectrum, we perform a global fit of the intensity maps presented in Fig. 3. For both maps we fit to a minimum number of exponentially decaying functions convolved with the Gaussian instrument response function, defined by the laser pulse cross-correlation. For both pump wavelengths we required two such functions.

To fit the 269 nm data we fix the time-zero of the exponentially decaying functions to be equal and find the best fit to have one component being described by the Gaussian instrument response function alone. The second component has an appreciable decay lifetime of ~30 fs. The DAS resulting from the fits are plotted in Fig. 5 (b). In Fig. 5 (a) we also plot a representative slice through the data at 10.25 eV to show the relative contributions of the two components to the photoelectron intensity. The exponential decay leads to a tail at longer delay times. The decay associated spectra are positive over the full range of energy values, suggesting that the population is decaying into some unmeasured state on an extremely rapid timescale. The enhanced signal over the course of the cross-correlation is due to the enhanced intensity driving a nonresonant multiphoton ionisation processes as seen in our previous experiments using the same methodology,[24] such that the dynamics of the system at this wavelength are defined by the 30 fs decay measured in the second component.

We take a slightly different approach for the data collected at 255 nm. The shifting energy features and changes in intensity mean the maximum is not always around time-zero. Fitting to exponentially decaying functions from the same initial time-zero does not provide a good fit to the data, such that we instead fit

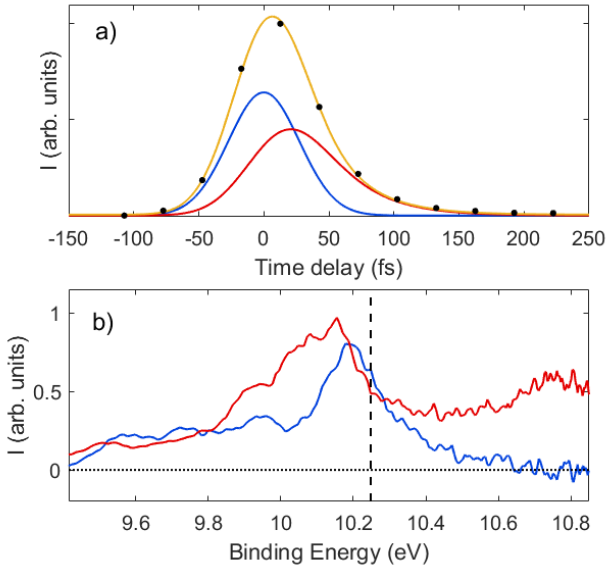

Fig. 5 (a) Results of the global fit (yellow) to the experimental data (black data points) for the 269 nm pump wavelength at the energy indicated by the dashed line in (b). The contribution from the two components of the fit are plotted with the Gaussian (fwhm∼65 fs) component in blue, and the exponentially decaying component with a lifetime of 30 fs plotted in red. (b) The decay associated spectra for the 269 nm data, with the blue line being the amplitude of the previously described Gaussian, and the red line being the amplitude for the exponentially decaying component.

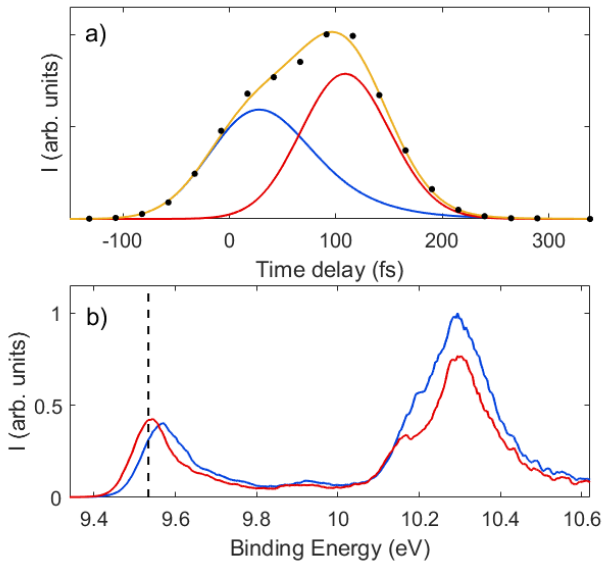

Fig. 6 (a) Results of the global fit (yellow) to the experimental data (black data points) for the 255 nm pump wavelength at the energy indicated by the dashed line in (b). The contribution from the two components of the fit are plotted with an exponentially decaying component with a lifetime of 40 fs (blue), and a 100 fs delayed component with a lifetime of 15 fs plotted in red. (b) The decay associated spectra for the 255 nm data, with the blue line being the amplitude of the initial component with a 40 fs lifetime, and the red line being the amplitude of the delayed component with a 15 fs lifetime.

the data to two Gaussian functions convolved with exponential decays and each with a variable time-zero that is fit to the data. The resulting DAS from this fit are plotted in Fig. 6 (b). In Fig. 6 (a) we also plot a representative slice through the data at 9.53 eV where the energy shift is perhaps most apparent and highlights the increased intensity at ∼100 fs after time-zero. The initial component centred at time-zero has an exponential lifetime of 40 fs, very close to the lifetime observed at 269 nm, while the second component is delayed by 100 fs and has a 15 fs lifetime. The physical origin of these timescales is somewhat harder to explicitly define but the relatively long time-delay to the second component in our model highlights the extended excited state lifetime when compared with the 269 nm pump data. The energy dependence of these two contributions is shown in Fig. 6 (b) where the peaks in the DAS are seen to shift to lower binding energy on the delayed component spectrum. The lack of shift in energy of the feature at 10.3 eV also adds validity to the origin of this feature being due to a resonant excitation of a Rydberg state during the ionisation process.

Discussion

The data presented in the preceding section shows significant wavelength dependence of the photoelectron signal suggesting large changes in the excited state lifetime and associated dynamics. This is surprising not only due to the small energy difference between the two pump wavelengths, but also due to the strongly repulsive nature of the excited state potentials shown in Fig. 1, where we would expect rapid disscociation regardless of the excited state populated.

Taking each pump wavelength in turn, at 269 nm we observe dynamics that are consistent with previous measurements in CH_3I. Excitation at this wavelength appears to be dominated by population of the $^3Q_0$ state. The ultrafast decay of excited state population is therefore indicative of the rapid, "ballistic", dissociation of the C-I bond along the $^3Q_0$ potential and the formation of $I(^2P_{1/2})$ fragment as previously observed with XUV transient absorption spectroscopy[3] and Coulomb explosion imaging[4] at similar pump wavelengths. We see no features that we can correlate with excitation of either the $^3Q_1$ or $^1Q_1$ states. This is unsurprising for the $^1Q_1$ state which, even for the most optimistic predictions, is not expected to have more than a few percent contribution to the overall wavepacket at this wavelength. The $^3Q_1$ is theoretically predicted to have a ∼10% contribution at this energy, but all experimental evidence to date suggests the contribution is much lower than this. Our observations are therefore consistent with previous experiments and we see no evidence for any population of the $^3Q_1$ state at 269 nm. It should be noted however that the dynamics on the $^3Q_1$ state may show very similar lifetimes to the $^3Q_0$ state such that the dynamic features could overlap. The lifetime measured for the departure of the initially excited wavepacket out of the ionisable Franck-Condon region is on the order of 30 fs and consistent with measurements of the formation of products.[1]

At a pump wavelength of 255 nm the situation is markedly different. The excitation fraction into the accessible exited states

is somewhat less clear. The experiments of Eppink and Parker[12] suggest that the population of the $^1Q_1$ state at 255 nm is much less than 1% with the remainder of the population being on the $^3Q_0$ state. MCD measurements[11] and theory,[14,19] however, give between 10-15%. In all cases the expected contribution from the $^3Q_1$ is expected to be minimal. The main difference between the two wavelengths therefore appears to be a potential increase in the contribution of the $^1Q_1$ state to the initial wavepacket.

Returning to the observed dynamics in the photoelectron spectrum: the shift in energy observed over the first 100 fs is indicative of a changing vibrational overlap between the excited state wavepacket and the accessible ion states. Typically for a dissociation reaction one would expect the shift to be to higher binding energies as the molecule moves to those associated with the neutral fragments. The shift to lower binding energy suggests the molecule is rearranging to be more aligned with the structure of the ground state of the ion, enhancing overlap with the lowest vibrational states, or that a component of the wavepacket that has higher overlap with the lower vibrational states is gaining importance relative to the other components that remain measurable. Combined with the shifts, we observe an increased excited state lifetime of >100 fs, compared with 30 fs lifetime measured at 269 nm. These two observations suggest a much more complex dynamic process is occurring at the same time as the direct dissociation process.

The data measured at 269 nm is indicative of rapid dissociation along the $^3Q_0$ potential which leads to a transient excited state population that remains observable for only a very short period of time, on the order of 30 fs. From the global fit it appears a similar process is occurring in the 255 nm pump data and is the most likely origin of the first decaying component in the fit. The secondary features associated with the delayed component are harder to assign, with the appearance and longer lifetime difficult to correlate with any of the known vibrational periods of the molecule. The shape of the $^3Q_0$ potential and the dependence on wavelength mean that it is unlikely that it is due to dynamics occurring on the $^3Q_0$ potential. We therefore suggest that these features are due to excited state population and dynamics on the $^1Q_1$ potential undergoing significant rearrangement prior to dissociation. The relatively high intensity of the delayed feature is in part a consequence of the lifetime dependent signal enhancement which amplifies the contribution of longer lifetime states through their convolution with the instrument response function[30]. The changes in Franck-Condon overlap which cause the shifts in energy also lead to an increase in signal intensity. The peak maximum of the long-lived component is therefore seen at later times than may be expected. The fit accounts for this shift by having a delayed "effective time-zero" for the long-lived component, corresponding to the delay in reaching the maximum intensity relative to the "real time-zero". The convolution of the non-negligible laser pulse duration on the intensity profiles leads to the well-known equations for the Gaussian convoluted with an exponential decay that form the basis functions for the global fit analysis described above.

Table 1 Percentage excitation fraction at the two wavelengths studied based on published experiment and theory

	255 nm			269 nm		
	$^3Q_0$	$^1Q_1$	$^3Q_1$	$^3Q_0$	$^1Q_1$	$^3Q_1$
Gedanken[11]	86.0%	14.0%	0%	96.7%	3.3%	0%
Eppink[12]	99.5%	0.5%	0%	100%	0%	0%
Bañares[14]	85.0%	15.0%	0%	81.7%	5.1%	13.3%
Alekseyev[19]	75.3%	23.9%	1.8%	81.6%	8.0%	10.3%

$$I(t) = Ne^{-\lambda t}e^{\frac{(\sigma\lambda)^2}{2}}\left(1+erf\left(\frac{(t-\sigma^2\lambda)}{(\sqrt{2}\sigma)}\right)\right) \quad (1)$$

Where I(t) is the time dependent intensity, λ is the rate constant associated with the exponential decay, σ defines the laser pulse cross-correlation width and N is a normalisation constant related to the laser pulse profile and absorption/ionisation cross-sections. The convolution leads to a lifetime dependent intensity enhancement that can amplify the contributions of states that have a longer lifetime relative to those with the same amplitude but shorter lifetimes. This lifetime dependent enhancement is quantifiable and was the subject of a recent set of numerical simulations that showed the effect over a range of pulse durations and excited state lifetimes.[30] With the parameters obtained from the global fit we can quantify the effect of this signal enhancement to obtain approximate population of the longer lived state relative to that with a shorter lifetime. Taking relative lifetimes on the order of 30 fs and 130 fs we can approximate the relative population of the secondary feature, assuming equal ionisation propensity, to be around 20% of the fast decaying component. For comparison with other measured and calculated distributions we present the percentage contribution of the 3 main states at the two wavelengths measured in table 1. From the table it is clear that the excitation fraction more closely matches those predicted by theory and MCD measurements, but much higher than those extrapolated from product angular distribution measurements (<1%).[12] So while the parallel transition remains dominant, the perpendicular state provides a significant but minor contribution to the dynamics on the blue edge. The dynamics on the $^1Q_1$ state, however, remain unclear based on the current measurements and available cuts across the potential energy surfaces[20,31] which do not provide any clues as to what could be causing the rather extended lifetime.

Summary

Using a multiphoton ionisation probe we have measured the initial dynamics of the methyl iodide molecule following UV excitation at two pump wavelengths. The dynamics observed are strikingly different, highlighting the subtle changes in dynamics in systems of apparent simplicity. To the red of the absorption maximum of the A-band, the dynamics match those expected based on previous measurements using a wide range of techniques. The rapid dissociation on the $^3Q_0$ state leads to a transient excited state population which has a measured lifetime of 30 fs. As the

pump photon energy is increased, the excited state population is no longer completely dominated by the $^3Q_0$ state and significant population of the $^1Q_1$ state is observed. The $^3Q_0$ component follows the same dynamic process and rapidly moves out of our observation window leading to dissociation on an ultrafast timescale. The population in the $^1Q_1$ state shows an extended lifetime and more complex dynamics.

Based on the observations, we can identify dynamic processes that increase the time the wavepacket remains within the observation window of the ionisation probe corresponding to bound structures of the methyl iodide molecule. The origin of the extra stability is hard to pinpoint based on cuts of the $^1Q_1$ potentials which show rather steep gradients towards dissociation products. Providing a more concrete analysis of the dynamics is a real challenge to experiment and theory. Based on cuts of the potential energy surfaces it is difficult to see what motion could extend the lifetime so significantly. Quantum dynamics calculations on full dimensional potential energy surfaces that account for the excitation process explicitly, and measurements covering the full dynamic process, are therefore essential if we are to obtain a better understanding of this and other complex systems. Full dimensional potential energy surfaces are available but do not accurately reproduce the absorption spectrum when all states are included.[32] Attempts by Alekseyev[19] to correct for this by shifting the position of states achieve moderate agreement but given the uncertainty in the position of the $^1Q_1$ state and the energy dependence of the observed dynamics it is unclear if this will reliably describe the dynamics. This gives significant uncertainty in the starting conditions for any dynamics calculation. Given the difficulty in calculating an accurate absorption spectrum for methyl iodide, calculating the dynamics and observables based on potential energy surfaces with sufficient accuracy to describe the energy dependence will provide a significant challenge. Advances in new spectroscopic probes based on XUV photoelectron spectroscopy,[23] X-ray absorption,[9] X-ray/electron scattering,[33,34] or Coulomb explosion imaging[4,8,10] allow for a complete measurement of the full process. The complexity of such measurements means that typically only a single pump wavelength is studied such that any subtle wavelength dependence is often left unmeasured. Strengthening the link between experimental observation and theoretical descriptions of the dynamics will therefore play a key role in unravelling the complex nature of dynamic processes resulting from complex excitations covering multiple interacting potential energy surfaces.

Acknowledgements

R. S. M. thanks the Royal Society for a University Research Fellowship (UFUF150655). R. S. M. and J. W. thank the EPSRC for funding (EP/R010609/1). B. D. W. thanks the Central Laser Facility and Chemistry at the University of Southampton for a studentship. E. W. thanks Chemistry at the University of Southampton for a studentship. A. K. acknowledges support from a Royal Society of Edinburgh Sabbatical Fellowship (58507) and a research grant from the Carnegie Trust for the Universities of Scotland (CRG050414). D. B. acknowledges an EPSRC studentship from the University of Edinburgh. We also acknowledge funding from the EC's Seventh Framework Programme (LASERLAB-EUROPE, grant agreement 228334). We thank John Dyke for very useful conversations and Phil Rice for technical assistance.

References

1 R. De Nalda, J. G. Izquierdo, J. Durá and L. Bañares, *J. Chem. Phys.*, 2007, **126**, 021101.

2 M. E. Corrales, V. Loriot, G. Balerdi, J. González-Vázquez, R. De Nalda, L. Bañares and A. H. Zewail, *Phys. Chem. Chem. Phys.*, 2014, **16**, 8812–8818.

3 A. R. Attar, A. Bhattacherjee and S. R. Leone, *J. Phys. Chem. Lett.*, 2015, **6**, 5072–5077.

4 F. Allum, M. Burt, K. Amini, R. Boll, H. Köckert, P. K. Olshin, S. Bari, C. Bomme, F. Brauße, B. Cunha de Miranda, S. Düsterer, B. Erk, M. Géléoc, R. Geneaux, A. S. Gentleman, G. Goldsztejn, R. Guillemin, D. M. P. Holland, I. Ismail, P. Johnsson, L. Journel, J. Küpper, J. Lahl, J. W. L. Lee, S. Maclot, S. R. Mackenzie, B. Manschwetus, A. S. Mereshchenko, R. Mason, J. Palaudoux, M. N. Piancastelli, F. Penent, D. Rompotis, A. Rouzée, T. Ruchon, A. Rudenko, E. Savelyev, M. Simon, N. Schirmel, H. Stapelfeldt, S. Techert, O. Travnikova, S. Trippel, J. G. Underwood, C. Vallance, J. Wiese, F. Ziaee, M. Brouard, T. Marchenko and D. Rolles, *J. Chem. Phys.*, 2018, **149**, 204313.

5 N. Thiré, R. Cireasa, V. Blanchet and S. T. Pratt, *Phys. Chem. Chem. Phys.*, 2010, **12**, 15644–15652.

6 J. Durá, R. de Nalda, J. Álvarez, J. G. Izquierdo, G. A. Amaral and L. Bañares, *ChemPhysChem*, 2008, **9**, 1245–1249.

7 J. Durá, R. de Nalda, G. A. Amaral and L. Bañares, *J. Chem. Phys.*, 2009, **131**, 134311.

8 K. Amini, E. Savelyev, F. Brauße, N. Berrah, C. Bomme, M. Brouard, M. Burt, L. Christensen, S. DÃijsterer, B. Erk, H. Höppner, T. Kierspel, F. Krecinic, A. Lauer, J. W. L. Lee, M. Müller, E. Müller, T. Mullins, H. Redlin, N. Schirmel, J. Thøgersen, S. Techert, S. Toleikis, R. Treusch, S. Trippel, A. Ulmer, C. Vallance, J. Wiese, P. Johnsson, J. Küpper, A. Rudenko, A. Rouzée, H. Stapelfeldt, D. Rolles and R. Boll, *Struct. Dyn.*, 2018, **5**, 014301.

9 F. Brauße, G. Goldsztejn, K. Amini, R. Boll, S. Bari, C. Bomme, M. Brouard, M. Burt, B. C. de Miranda, S. Düsterer, B. Erk, M. Géléoc, R. Geneaux, A. S. Gentleman, R. Guillemin, I. Ismail, P. Johnsson, L. Journel, T. Kierspel, H. Köckert, J. Küpper, P. Lablanquie, J. Lahl, J. W. L. Lee, S. R. Mackenzie, S. Maclot, B. Manschwetus, A. S. Mereshchenko, T. Mullins, P. K. Olshin, J. Palaudoux, S. Patchkovskii, F. Penent, M. N. Piancastelli, D. Rompotis, T. Ruchon, A. Rudenko, E. Savelyev, N. Schirmel, S. Techert, O. Travnikova, S. Trippel, J. G. Underwood, C. Vallance, J. Wiese, M. Simon, D. M. P. Holland, T. Marchenko, A. Rouzée and D. Rolles, *Phys. Rev. A*, 2018, **97**, 043429.

10 M. E. Corrales, J. González-Vázquez, R. de Nalda and L. Bañares, *J. Phy. Chem. Lett.*, 2019, **10**, 138–143.

11 A. Gedanken and M. D. Rowe, *Chem. Phys. Lett.*, 1975, **34**, 39 – 43.

12 A. T. J. B. Eppink and D. H. Parker, *J. Chem. Phys.*, 1998, **109**,

4758–4767.
13 A. T. J. B. Eppink and D. H. Parker, *J. Chem. Phys.*, 1999, **110**, 832–844.
14 L. Rubio-Lago, A. García-Vela, A. Arregui, G. A. Amaral and L. Bañares, *J. Chem. Phys.*, 2009, **131**, 174309.
15 M. G. González, J. D. Rodríguez, L. Rubio-Lago, A. García-Vela and L. Bañares, *Phys. Chem. Chem. Phys.*, 2011, **13**, 16404 – 16415.
16 D. Imre, J. L. Kinsey, A. Sinha and J. Krenos, *J. Phys. Chem.*, 1984, **88**, 3956–3964.
17 S. M. Poullain, D. V. Chicharro, L. Rubio-Lago, A. García-Vela and L. Bañares, *Phil. Trans. R. Soc. A*, 2017, **375**, 20160205.
18 R. S. Mulliken, *J. Chem. Phys*, 1940, **8**, 382.
19 A. B. Alekseyev, H.-P. Liebermann and R. J. Buenker, *J. Chem. Phys.*, 2007, **126**, 234103.
20 A. B. Alekseyev, H.-P. Liebermann, R. J. Buenker and S. N. Yurchenko, *J. Chem. Phys.*, 2007, **126**, 234102.
21 S. Marggi Poullain, D. V. Chicharro, J. González-Vázquez, L. Rubio-Lago and L. Bañares, *Phys. Chem. Chem. Phys.*, 2017, **19**, 7886–7896.
22 A. R. Bainbridge, J. Harrington, A. Kirrander, C. Cacho, E. Springate, W. A. Bryan and R. S. Minns, *New J. Phys.*, 2015, **17**, 103013.
23 A. D. Smith, E. M. Warne, D. Bellshaw, D. A. Horke, M. Tudorovskya, E. Springate, A. J. H. Jones, C. Cacho, R. T. Chapman, A. Kirrander and R. S. Minns, *Phys. Rev. Lett.*, 2018, **120**, 183003.
24 A. D. Smith, H. M. Watts, E. Jager, D. A. Horke, E. Springate, O. Alexander, C. Cacho, R. T. Chapman and R. S. Minns, *Phys. Chem. Chem. Phys.*, 2016, **18**, 28150–28156.
25 D. Irimia, D. Dobrikov, R. Kortekaas, H. Voet, D. A. van den Ende, W. A. Groen and M. H. M. Janssen, *Rev. Sci. Instrum.*, 2009, **80**, 113303.
26 S. P. Goss, D. C. McGilvery, J. D. Morrison and D. L. Smith, *J. Chem. Phys.*, 1981, **75**, 1820–1828.
27 W. A. Chupka, S. D. Colson, M. S. Seaver and A. M. Woodward, *Chem. Phys. Lett.*, 1983, **95**, 171 – 176.
28 E. M. Warne, B. Downes-Ward, J. Woodhouse, M. A. Parkes, D. Bellshaw, E. Springate, P. Majchrzak, P. Pearcy, Y. Zhang, G. Karras, A. Wyatt, R. T. Chapman, A. Kirrander and R. S. Minns, *In Preparation*, 2019.
29 S. Eden, P. Limão-Vieira, S. V. Hoffmann and N. J. Mason, *Chem. Phys.*, 2007, **331**, 232–244.
30 N. Kotsina and D. Townsend, *Phys. Chem. Chem. Phys.*, 2017, **19**, 29409–29417.
31 N. Wittenbrink and W. Eisfeld, *J. Chem. Phys.*, 2018, **148**, 094102.
32 C. R. Evenhuis and U. Manthe, *The Journal of Physical Chemistry A*, 2011, **115**, 5992–6001.
33 M. P. Minitti, J. M. Budarz, A. Kirrander, J. S. Robinson, D. Ratner, T. J. Lane, D. Zhu, J. M. Glownia, M. Kozina, H. T. Lemke, M. Sikorski, Y. Feng, S. Nelson, K. Saita, B. Stankus, T. Northey, J. B. Hastings and P. M. Weber, *Phys. Rev. Lett.*, 2015, **114**, 255501.
34 J. Yang, X. Zhu, T. J. A. Wolf, Z. Li, J. P. F. Nunes, R. Coffee, J. P. Cryan, M. Gühr, K. Hegazy, T. F. Heinz, K. Jobe, R. Li, X. Shen, T. Veccione, S. Weathersby, K. J. Wilkin, C. Yoneda, Q. Zheng, T. J. Martinez, M. Centurion and X. Wang, *Sci.*, 2018, **361**, 64–67.